

# The fracture strength of $\text{AlLiB}_{14}$

L. F. Wan<sup>1</sup> and S. P. Beckman<sup>1,\*</sup>

<sup>1</sup>*Department of Material Science and Engineering, Iowa State University, Ames, Iowa 50014, USA*  
(Dated: June 12, 2018)

The orthorhombic boride crystal family  $\text{XYB}_{14}$ , where X and Y are metal atoms, plays a critical role in a unique class of superhard compounds, yet there have been no studies aimed at understanding the origin of the mechanical strength of this compound. We present here the results from a comprehensive investigation into the fracture strength of the archetypal  $\text{AlLiB}_{14}$  crystal. First-principles, *ab initio*, methods are used to determine the ideal brittle cleavage strength for several high-symmetry orientations. The elastic tensor and the orientation-dependent Young's modulus are calculated. From these results the lower bound fracture strength of  $\text{AlLiB}_{14}$  is predicted to be between 29 and 31 GPa, which is near the measured hardness reported in the literature. These results indicate that the intrinsic strength of  $\text{AlLiB}_{14}$  is limited by the interatomic B–B bonds that span between the B layers.

The development of new superhard materials that can operate under extreme conditions is critical for high-performance industrial manufacturing and is a subject that has recently received great attention. [1–3] The orthorhombic borides, formulated as  $\text{XYB}_{14}$  where X and Y are metal atoms, have been of interest to scientists and engineers for the past decade due to a report [4, 5] that  $\text{AlMgB}_{14}$  prepared by mechanical milling can achieve a hardness between 32 and 46 GPa. The reason for the observed superhardness is not understood. It is suggested that in part the strength is due to the so-called “nanocomposite” microstructure comprised of  $\text{AlMgB}_{14}$  and  $\text{TiB}_2$ , although the hardness of each individual phase is believed to be less than the hardness of the composite. [6] There have been many studies examining  $\text{TiB}_2$ , [7–10] but the orthorhombic boride family has received much less attention and is therefore the focus of this letter.

Whereas most hard materials are dense, highly-symmetric crystals, the  $\text{XYB}_{14}$  structure, shown in Fig. 1, is relatively open and has low symmetry ( $\text{Imma}$ ). This crystal structure, which was first reported by Matkovich and Economy in 1970, has a unit cell containing four formula units of  $\text{XYB}_{14}$ . [11] The 64-atom unit cell can be expressed as  $\text{X}_4\text{Y}_4(\text{B}_{12})_4\text{B}_8$  to distinguish the two B allotropes. The B layers are constructed from  $\text{B}_{12}$  icosahedron that are connected to each other through the so-called inter-icosahedra B atoms that are trigonally bonded to three  $\text{B}_{12}$  units within the B layer. Recent spectroscopy evidence indicates that the B–B bonds that span between the B layers, directly connecting icosahedron, are very strong. [12] Unlike many metal-boride compounds the metal atoms are not covalently bonded to the B, but instead the metal atoms ionize and donate their valence electrons to the covalently bonded B network. [13–16] As a near-superhard material, this crystal family is unique, which has led us to investigate the bonding in the crystal as it affects the crystal's mechanical strength.

Following Matkovich and Economy's work, [11] Higashi and Ito synthesized several  $\text{XYB}_{14}$  compounds and used

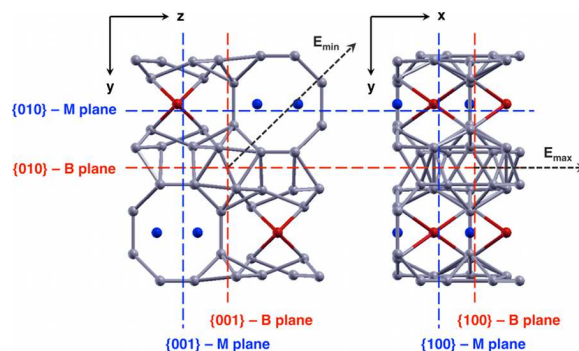


FIG. 1. (color online) A simple schematic of the  $\text{XYB}_{14}$  crystal structure. The red (medium grey) spheres are the X-site, the blue (dark grey) spheres are the Y-site, and the light grey spheres are the B atoms. The short-dashed arrows denoted by  $E_{\min}$  and  $E_{\max}$  show the loading directions that yield the minimum and maximum Young's modulus for  $\text{AlLiB}_{14}$ . The six planes selected for examination within the brittle cleavage model are shown as long-dashed lines and are labeled according to the nomenclature used in Table I.

diffraction methods to refine the crystallographic data. For some of the compounds, such as  $\text{AlMgB}_{14}$ , a relatively high concentration of vacancies, around 25%, are found at the metal atom sites. [17] Diffraction results for other  $\text{XYB}_{14}$  compounds, such as  $\text{AlLiB}_{14}$ , do not find such a large number of vacancies. [18, 19] Werheit *et al.* have used Raman spectroscopy to compared the vibrational spectrum of various  $\text{XYB}_{14}$  compounds and have found that the  $\text{AlLiB}_{14}$  crystal has less internal distortions than many other  $\text{XYB}_{14}$  structures, including  $\text{AlMgB}_{14}$ . [12] From these results we conclude that experimental specimens of  $\text{AlLiB}_{14}$  are likely to have fewer point defects than many other  $\text{XYB}_{14}$  compounds and consequently  $\text{AlLiB}_{14}$  is selected as the archetypal structure for study in this letter.

Previous theoretical studies have focused on the effects of chemical substitution on the properties of the  $\text{XYB}_{14}$  crystal family. [13–15, 20] This is in part because the sys-

tem is known to accept a large number of metal species including Li, Be, Na, Mg, Al, as well as a variety of rare-earth elements, such as Tb, Dy, Ho, Er, Yb, and Lu. [4, 18, 19, 21–24] In addition the superhard Ames Lab specimen was synthesized by a mechanical alloying method, which introduces a wide variety of impurity species to the crystal including Ti, Si, Fe, O, and C. [5] In these theoretical studies the reported figure of merit for hardness is the bulk modulus because its computation is relatively simple. However, the bulk modulus alone only gives information about the average bond strength under an applied volume dilation and does not give any information about the strength of individual bonds in the crystal. Understanding hardness requires knowledge about the local mechanisms for bond breaking as it relates to fracture in the crystal. In this letter the fracture strength of  $\text{AlLiB}_{14}$  will be examined using an ideal brittle cleavage model. This approach allows for insight regarding the local bonding within the crystal and may lead to a strategy for improving the hardness.

The first-principles, density functional theory method used in this study is implemented in the SIESTA software package. [25, 26] The Perdew-Burke-Ernzerhof generalized gradient approximation (GGA) is used for the exchange-correlation energy and norm-conserving pseudopotentials are used in place of the all-electron atomic potentials. [27, 28] The wavefunction is represented by a set of finite-range numerical atomic orbitals. Each atomic basis is extended to include double- $\zeta$  functions plus a shell polarization that is constructed using the split-valence scheme. [29] The cutoff radii used for each  $\zeta$  function are presented in Ref. 30. Real space meshing is performed to an energy cutoff of 175 Rydberg. The Kohn-Sham energies are sampled across the Brillouin zone using a  $12 \times 12 \times 12$  Monkhorst-Pack grid. [31] The atomic structural optimization follows the conjugate gradient minimization method and the thresholds for the residual forces on atoms and the supercell are  $0.005 \text{ eV/\AA}$  and  $0.0005 \text{ eV/\AA}^3$  respectively. The calculated lattice parameters for  $\text{AlLiB}_{14}$  are 5.88, 10.39, and 8.15  $\text{\AA}$ , which agree well with the reported experimental values 5.847, 10.354, and 8.143  $\text{\AA}$ . [18]

The ideal brittle cleavage model used here separates the  $\text{AlLiB}_{14}$  crystal into two semi-infinite, rigid atomic blocks that are pulled apart to introduce a pair of cleavage surfaces at a predefined atomic plane. This idealized approach simultaneously stretches and breaks all the bonds at the interface. Although the effect of crack tip initiation and propagation cannot be included using this method, it allows for the bond strengths localized in the crystal to be investigated. Internal atomic relaxations and lattice contractions perpendicular to the direction of elongation are forbidden. These constraints allow the strength of the bonds across the cleavage interface to be determined independent of possible near-surface atomic reconstructions, which would be present in an experi-

TABLE I. The numerical results for applying the ideal brittle cleavage model to the six  $\text{AlLiB}_{14}$  cleavage planes that are shown in Fig. 1.

Orientation	Cleavage energy	Critical length	Critical stress
	$G_b/\text{Area}$ ( $\text{J/m}^2$ )	$l_b$ ( $\text{\AA}$ )	$\sigma_b$ (GPa)
{100}–B	7.94	0.51	57.7
{100}–M	7.74	0.45	63.5
{010}–B	9.16	0.49	68.4
{010}–M	5.42	0.56	35.7
{001}–B	8.27	0.49	62.0
{001}–M	7.51	0.57	48.1

mental specimen. The calculated energy of the cleaved crystal, relative to the energy of the perfect crystal, is called the decohesive energy,  $E_b$ , and is determined as a function of the interplaner spacing,  $x$ , across the specified cleavage planes. The decohesive energy is fit to the universal binding energy relation (UBER) developed by Rose *et al.* in Ref. 32, which is expressed more precisely in Ref. 33 as,

$$E_b(x) = G_b \left[ 1 - \left( 1 + \frac{x}{l_b} \right) \exp \left( -\frac{x}{l_b} \right) \right].$$

When all the atomic bonds that span the cleavage interface are broken, the decohesive energy saturates to the cleavage energy,  $G_b$ . The cleavage stress is the first derivative of the decohesive energy with respect to  $x$ . The critical cleavage stress,  $\sigma_b$ , is defined as the maximum stress, and the corresponding interplanar spacing is referred to as the critical length,  $l_b$ .

For  $\text{AlLiB}_{14}$  cleavage is considered within the high-symmetry {100}, {010}, and {001} families of planes. For each crystallographic direction two cleavage planes are examined: one that passes through the icosahedron, labeled “B,” and one that passes between the icosahedron, labeled “M.” These were selected to best represent the variation in the bonding for each of the sampled directions; one of the cleavage planes has many bonds that span the interface and the other few bonds. It is intended to test interfaces with the highest and lowest fracture energies. These planes are identified in Fig. 1. A 128-atom supercell is used to guarantee that the calculated decohesive energies are converged to better than  $0.005 \text{ J/m}^2$ . The decohesive energies, UBER fit, and derived stresses are plotted in Fig. 2. The computed data matches the functional form of the UBER relation very well and the resulting critical parameters are listed in Table I.

The decohesive energy curves and stresses for the {100}–B and –M planes are very similar, the critical

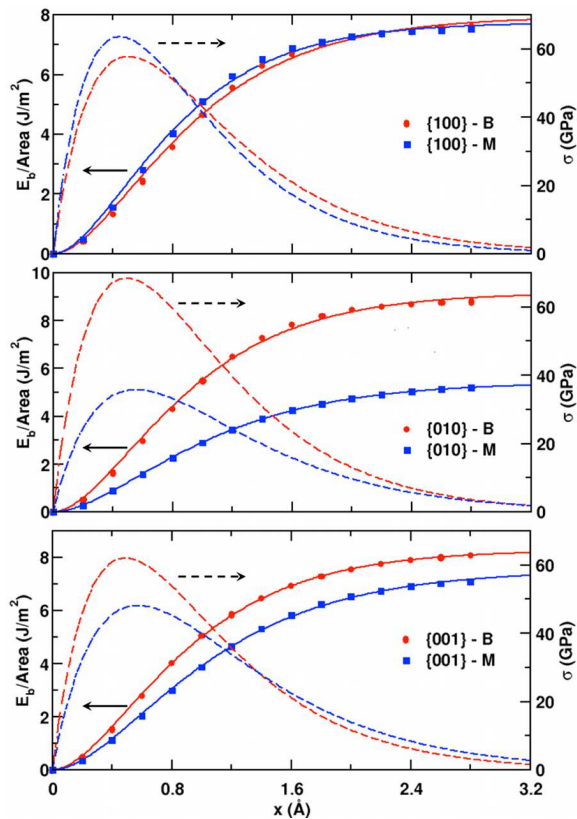


FIG. 2. (color online) The ideal brittle cleavage results for  $\text{AlLiB}_{14}$ . The left ordinate axis labels the energies and the right the stresses. The top frame gives the results for the  $\{100\}$  planes, the middle the  $\{010\}$  planes, and the bottom the  $\{001\}$  planes. In each frame the “B” results are red (light grey) and the “M” results are blue (dark grey). The decohesive energy DFT data are solid symbols, the UBER relations are solid lines, and the stresses are dashed lines.

stresses differ by less than 10%. This is not surprising considering that the density and geometric arrangements of the B–B bonds in these planes are nearly equivalent. Whereas the  $\{100\}$  planes are very similar, the  $\{010\}$  planes are considerably different. The  $\{010\}$ –B plane passes through the B layer bisecting the icosahedron, breaking many B–B bonds, but the  $\{010\}$ –M plane passes between the B layers and therefore cuts significantly fewer bonds. Within the ideal brittle cleavage model the calculated critical stress for the M plane is 48% smaller than that of the B plane.

According to the Raman spectroscopy results reported in Ref. 12, the B–B bonds that span between the B layers and connect the icosahedron are expected to have a greater binding strength than the bonds inside the icosahedron. This can be examined qualitatively by plotting the bonding charge density, as shown in Fig. 3. [34] The bonding process results in a buildup of charge in the B–B bonds that bridge the B layers. In Fig. 3 charge accumulation between the B layers is observed both between the

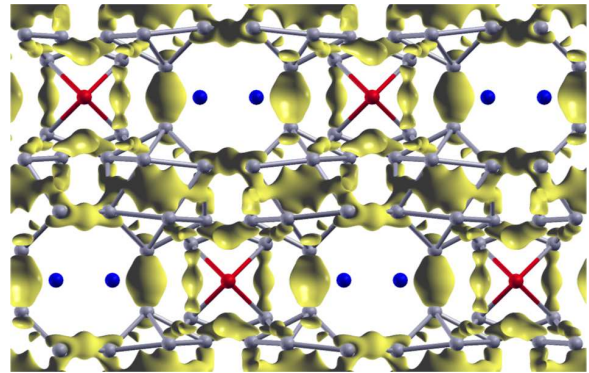


FIG. 3. (online color) An isosurface showing regions in an  $\text{XYB}_{14}$  crystal with positive bonding charge density. The atomic sites are color coded following the description in Fig. 1.

icosahedron and the inter-icosahedra B. The results from the ideal cleavage model, presented in Table I, indicate that regardless of the anticipated high strength of the bonds at this plane, the relatively low number density of bonds causes the  $\{010\}$ –M plane to have the lowest critical stress of all the planes examined here. It can be concluded that the B–B bonds that span between the B layers are key for controlling the overall strength of the crystal.

It is the weakest planes that are of primary interest because fracture naturally transverses the weakest path through a crystal. It is these same planes that also dominate the elastic response. For a given family of planes, the elastic response to a uniaxial load applied normal to the planes should be an indicator of the relative cleavage strength, *i.e.*, the Young’s modulus should scale with the cleavage strength. For the orthorhombic  $\text{XYB}_{14}$ -type crystal there are nine unique tensor elements that can be derived from the linear stress-strain relation and the crystal symmetries. The components of the stiffness and compliance tensors for  $\text{AlLiB}_{14}$  are calculated and presented in Table II. In Fig. 4(a), the Young’s modulus,  $E$ , is represented as a function of crystallographic orientation, according to the formula,

$$\frac{1}{E} = l_1^4 s_{11} + l_2^4 s_{22} + l_3^4 s_{33} + 2l_1^2 l_2^2 s_{12} + 2l_1^2 l_3^2 s_{13} + 2l_2^2 l_3^2 s_{23} + l_2^2 l_3^2 s_{44} + l_1^2 l_3^2 s_{55} + l_1^2 l_2^2 s_{66},$$

where  $s_{ij}$  are the elastic compliance tensor components and  $l_1$ ,  $l_2$ , and  $l_3$  are the direction cosines. The representation surface in Fig. 4(a) is projected on the (100), (010) and (001) planes, and the results are shown in Fig. 4(b).

For the [010], [001], and [100] directions the Young’s modulus is 293, 404 and 505 GPa. From the ideal brittle cleavage model the minimum critical stresses for these same directions are 35.7, 48.1, and 57.7 GPa, as listed in Table I. Comparing these numbers demonstrates that indeed the directional representation of the Young’s modulus is an accurate predictor of the relative ideal fracture

TABLE II. The elastic tensor components for  $\text{AlLiB}_{14}$ .

Stiffness coefficients (GPa)	$c_{11}$	$c_{22}$	$c_{33}$	$c_{44}$	$c_{55}$	$c_{66}$	$c_{12}$	$c_{13}$	$c_{23}$
	526	411	419	91.0	201	130	45.7	83.4	32.0
Compliance coefficients ( $\times 10^{-12} \text{m}^2/\text{N}$ )	$s_{11}$	$s_{22}$	$s_{33}$	$s_{44}$	$s_{55}$	$s_{66}$	$s_{12}$	$s_{13}$	$s_{23}$
	1.98	2.47	2.47	10.99	4.98	7.69	-0.19	-0.38	-0.15

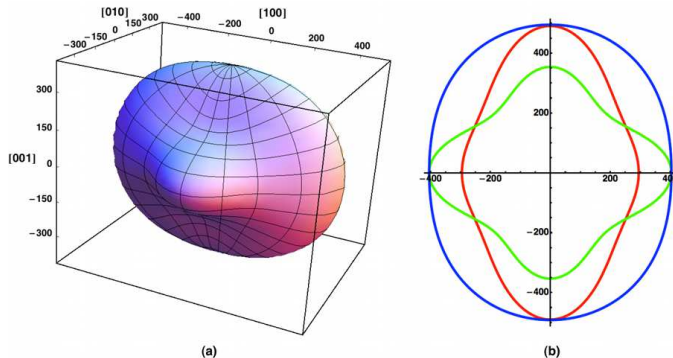


FIG. 4. (color online) The representation surface for the Young's modulus of  $\text{AlLiB}_{14}$  (given in GPa) as a function of crystallographic orientation. Frame (a) shows a 3D plot of the representation surface. Frame (b) shows 2D projections of the representation surface onto the (100), (010) and (001) planes and are printed in green (light grey), blue (dark grey), and red (medium grey) respectively.

strength of a particular orientation. From the results in Fig. 4 the minimum value of the Young's modulus is 256.0 GPa, which corresponds to a uniaxial load orientated ( $\phi = 90^\circ$ ,  $\theta = 44.96^\circ$ ), where  $\phi$  is the angle of rotation from the positive  $x$ -axis to the positive  $y$ -axis in the  $xy$ -plane and  $\theta$  is the out-of-plane angle of rotation from the positive  $z$ -axis to the  $xy$ -plane. This direction is drawn in Fig. 1 as a short-dashed arrow that is labeled  $E_{\min}$ . Assuming linear proportional scaling, the computed results for the high-symmetry orientations can be used to predict that the cleavage strength for a uniaxial load applied in the  $E_{\min}$  direction is between 29 and 31 GPa. This is the predicted lower limit of the ideal brittle cleavage strength for  $\text{AlLiB}_{14}$ . We submit that for a brittle material, such as  $\text{AlLiB}_{14}$ , which does not undergo extensive plastic deformation near the crack tip prior to fracture, the calculated ideal brittle cleavage strength is a reasonable estimation of the fracture strength. The physical features of fracture neglected in this ideal brittle cleavage model, including crack tip plasticity, lattice contractions, and atomic reconstructions, results in an overestimation of the cleavage energy and subsequently the actual critical energy and stress will be lower than our calculated results. The experimentally measured hardness for  $\text{AlLiB}_{14}$  ranges between 20 and

29 GPa [18, 21], which suggests that for this material the atomic scale behavior that we have reported here plays an important role in determining the actual hardness of the material.

In summary, we have coupled the results from a series of ideal brittle cleavage strength calculations to the calculated orientation dependent Young's modulus to predict the fracture strength of  $\text{AlLiB}_{14}$ . While admittedly this simplistic model neglects some of the macroscopic features of fracture associated with crack-tips, lattice plasticity, and interface reconstructions, we believe that here we have demonstrated that this still may be an effective approach to gauge the strength of brittle materials, such as the  $\text{XYB}_{14}$  crystal family. In contrast to all of the previous theoretical studies of the  $\text{XYB}_{14}$  crystal family, which have used the bulk modulus as an indicator of the bond strength, the approach used here allows for the local bond strength to be investigated on a plane-by-plane basis. Unlike the more sophisticated, multi-scale modeling approaches, which have been deployed to study fracture in polycrystalline diamond, Si, and other metallic systems, [35–38] the method used here is relatively simple. We believe that our approach can be used to screen prospective structures prior to their being investigated using a more elaborate theoretical technique.

The existing picture of bonding in the  $\text{XYB}_{14}$  crystal family is that B forms a covalent network of atoms constructed of  $\text{B}_{12}$  icosahedron. The  $\text{B}_{12}$  are stabilized by the electrons donated by the ionized metal atoms, according to the Jemmis mno rules. [39] Excess charge accumulates in the inter-icosahedra bonds, both those within the B layer and those that span between the layers. Experimental results indicate that the inter-icosahedra B–B bonds spanning between the layers are stronger than the intra-icosahedra bonds. [12] Here we find that regardless the strength of the inter-icosahedra bonds the fracture is significantly more likely to proceed between the icosahedron rather than through, due to the density of bonds at the cleavage plane. In fact the  $\{010\}$ -M planes are the weakest of those examined in this study, which suggests that the hardness of the material may be closely tied to the B–B bonding that connects the icosahedra layers. In practice, this means the intrinsic strength of this crystal family possibly can be changed, either strengthened or weakened, by the introduction of a dopant species that

directly affects these bonds.

The authors gratefully acknowledge financial support from the National Science Foundation through grant DMR-1105641.

---

\* sbeckman@iastate.edu.

- [1] R. B. Kaner, J. J. Gilman, and S. H. Tolbert, *Science* **308**, 1268 (2005).
- [2] V. L. Solozhenko, D. Andrault, G. Fiquet, M. Mezouar, and D. C. Rubie, *Appl. Phys. Lett.* **78**, 1385 (2001).
- [3] P. F. McMillan, *Nat. Mater.* **1**, 19 (2002).
- [4] B. A. Cook, J. L. Harringa, T. L. Lewis, and A. M. Russell, *Scripta Mater.* **42**, 597 (2000).
- [5] T. L. Lewis, “A study of selected properties and applications of almg14 and related composites: Ultra-hard materials,” (2001).
- [6] A. Ahmed, S. Bahadur, B. A. Cook, and J. Peters, *Tribol. Int.* **39**, 129 (2006).
- [7] R. G. Munro, *J. Res. Natl. Inst. Stand. Technol.* **105**, 709 (2000).
- [8] P. S. Spoor, J. D. Maynard, M. J. Pan, D. J. Green, J. R. Hellmann, and T. Tanaka, *Appl. Phys. Lett.* **70**, 1959 (1997).
- [9] N. L. Okamoto, M. Kusakari, K. Tanaka, H. Inui, and S. Otani, *Acta Mater.* **58**, 76 (2010).
- [10] R. Heid, B. Renker, H. Schober, P. Adelman, D. Ernst, and K.-P. Bohnen, *Phys. Rev. B* **67**, 180510 (2003).
- [11] V. I. Matkovich and J. Economy, *J. Acta Cryst.* **26**, 616 (1970).
- [12] H. Werheit, V. Filipov, U. Kuhlmann, U. Schwarz, M. Armbruster, A. Leithe-Jasper, T. Tanaka, I. Higashi, T. Lundstrom, V. N. Gurin, and M. M. Korsukova, *Sci. Technol. Adv. Mater.* **11**, 023001 (2010).
- [13] Y. Lee and B. N. Harmon, *J. Alloy Compd.* **338**, 242 (2002).
- [14] H. Kölpin, D. Music, G. Henkelman, and J. M. Schneider, *Phys. Rev. B* **78**, 054122 (2008).
- [15] L. F. Wan and S. P. Beckman, *Mater. Lett.* **74**, 5 (2012).
- [16] L. F. Wan and S. P. Beckman, *IOP Conf. Ser.: Mater. Sci. Eng.* **18**, 082024 (2011).
- [17] I. Higashi and T. Ito, *J. Less-Common Met.* **92**, 239 (1983).
- [18] I. Higashi, S. Kobayashi, M. Okada, K. Hamano, and T. Lundstrom, *J. Cryst. Growth* **128**, 1113 (1993).
- [19] J. S. Peters, J. M. Hill, and A. M. Russell, *Scripta Mater.* **54**, 813 (2006).
- [20] R. Sahara, T. Shishido, A. Nomura, K. Kudou, S. Okada, V. Kumar, K. Nakajima, and Y. Kawazoe, *J. Phys.: Conference Series* **176**, 012018 (2009).
- [21] K. Kudou, S. Okada, T. Mori, K. Iizumi, T. Shishido, T. Tanaka, I. Higashi, P. R. K. Nakajima, Y. B. Andersson, and T. Lundström, *Jpn. J. Appl. Phys.* **41**, 928 (2002).
- [22] S. Okada, T. Tanaka, A. Sato, T. Shishido, K. Kudou, K. Nakajima, and T. Lundstrom, *J. Alloys Compd.* **395**, 231 (2005).
- [23] M. M. Korsukova, V. N. Gurin, Y. B. Kuzma, N. F. Chaban, S. I. Chykhrii, V. V. Moshchalkov, N. B. Brandt, A. A. Gippius, and H. N. Ho, *Phys. Status Solidi. A* **114**, 265 (1989).
- [24] M. M. Korsukova, V. N. Gurin, Y. Yu, L. E. Tergenius, and T. Lundstrom, *J. Alloys Compd.* **190**, 185 (1993).
- [25] W. Kohn and L. J. Sham, *Phys. Rev.* **140**, A1133 (1965).
- [26] J. M. Soler, E. Artacho, J. D. Gale, A. Garcia, J. Junquera, P. Ordejon, and D. Sanchez-Portal, *J. Phys.: Condens. Matter* **14**, 2745 (2002).
- [27] J. P. Perdew, K. Burke, and M. Ernzerhof, *Phys. Rev. Lett.* **77**, 3865 (1996).
- [28] N. Troullier and J. L. Martins, *Phys. Rev. B* **43**, 1993 (1991).
- [29] J. Junquera, O. Paz, D. Sanchez-Portal, and E. Artacho, *Phys. Rev. B* **64**, 235111 (2001).
- [30] L. F. Wan and S. P. Beckman, in preparation (2012).
- [31] H. J. Monkhorst and J. D. Pack, *Phys. Rev. B* **13**, 5188 (1976).
- [32] J. H. Rose, J. R. Smith, and J. Ferrante, *Phys. Rev. B* **28**, 1835 (1983).
- [33] P. Lazar, R. Podloucky, and W. Wolf, *Appl. Phys. Lett.* **87**, 261910 (2005).
- [34] The bonding charge density is rendered by subtracting the charge density of the bonded structure from the sum of the charge contribution from each of the atoms, treated as though they are isolated. A positive bonding charge density indicates charge accumulation and a negative value indicates charge depletion.
- [35] O. A. Shenderova, D. W. Brenner, A. Omeltchenko, X. Su, and L. H. Yang, *Phys. Rev. B* **61**, 3877 (2000).
- [36] F. F. Abraham, J. Q. Broughton, N. Bernstein, and E. Kaxiras, *Europhys. Lett.* **44**, 783 (1998).
- [37] P. Gumbsch and G. E. Beltz, *Modeling Simul. Mater. Sci. Eng.* **3**, 597 (1995).
- [38] W. A. Curtin and R. E. Miller, *Modeling Simul. Mater. Sci. Eng.* **11**, R33 (2003).
- [39] E. E. Jemmis and M. M. Balakrishnarajan, *B. Mater. Sci.* **22**, 863 (1999).